

VIMS Articles

2017

The origins of the anomalous warming in the California coastal ocean and San Francisco Bay during 2014-2016

Yi Chao

Remote Sensing Solutions

Et al.

Yinglong J. Zhang

Virginia Institute of Marine Science, yjzhang@vims.edu

Follow this and additional works at: <https://scholarworks.wm.edu/vimsarticles>



Part of the [Marine Biology Commons](#)

Recommended Citation

Chao, Yi; Et al.; and Zhang, Yinglong J., "The origins of the anomalous warming in the California coastal ocean and San Francisco Bay during 2014-2016" (2017). *VIMS Articles*. 242.

<https://scholarworks.wm.edu/vimsarticles/242>

This Article is brought to you for free and open access by W&M ScholarWorks. It has been accepted for inclusion in VIMS Articles by an authorized administrator of W&M ScholarWorks. For more information, please contact scholarworks@wm.edu.

RESEARCH ARTICLE

10.1002/2017JC013120

Special Section:

The U.S. IOOS Coastal and Ocean Modeling Testbed 2013-2017

Key Points:

- Observations and model heat budget analyses show warming to be a result of propagation of signals from the west (Blob) and south (El Niño)
- Results from model sensitivity experiments support the conclusions drawn from the heat budget analyses
- The relatively slow propagation of the remote signals means that such warming events may be predictable months in advance

Correspondence to:

J. D. Farrara,
jfarrara@remotesensingsolutions.com

Citation:

Chao, Y., et al. (2017), The origins of the anomalous warming in the California coastal ocean and San Francisco Bay during 2014–2016, *J. Geophys. Res. Oceans*, 122, 7537–7557, doi:10.1002/2017JC013120.










Received 22 MAY 2017

Accepted 21 AUG 2017

Accepted article online 25 AUG 2017

Published online 18 SEP 2017

The origins of the anomalous warming in the California coastal ocean and San Francisco Bay during 2014–2016

Yi Chao^{1,2} , John D. Farrara¹ , Eric Bjorkstedt³, Fei Chai⁴, Francisco Chavez⁵ , Daniel L. Rudnick⁶ , Wendy Enright⁷ , Jennifer L. Fisher⁸, William T. Peterson⁹ , Gregory F. Welch⁷, Curtiss O. Davis¹⁰, Richard C. Dugdale¹¹ , Frances P. Wilkerson¹¹ , Hongchun Zhang², Yinglong Zhang¹² , and Eli Ateljevich¹³

¹Remote Sensing Solutions, Monrovia, California, USA, ²Joint Institute for Regional Earth System Science and Engineering, University of California, Los Angeles, California, USA, ³Southwest Fisheries Science Center, NOAA, Trinidad, California, USA, ⁴School of Marine Sciences, University of Maine, Orono, Maine, USA, ⁵Monterey Bay Aquarium Research Institute, Moss Landing, California, USA, ⁶Scripps Institution of Oceanography, University of California, San Diego, California, USA, ⁷City of San Diego Marine Biology Laboratory, Public Utilities Department, San Diego, California, USA, ⁸Cooperative Institute for Marine Resources Studies, Hatfield Marine Science Center, Oregon State University, Newport, Oregon, USA, ⁹Northwest Fisheries Science Center, NOAA, Hatfield Marine Science Center, Newport, Oregon, USA, ¹⁰College of Earth, Ocean and Atmospheric Sciences, Oregon State University, Corvallis, Oregon, USA, ¹¹Romberg Tiburon Center, San Francisco State University, Tiburon, California, USA, ¹²Virginia Institute of Marine Science, Gloucester Point, Virginia, USA, ¹³Bay-Delta Office, Department of Water Resources, Sacramento, California, USA

Abstract During 2014 exceptionally warm water temperatures developed across a wide area off the California coast and within San Francisco Bay (SFB) and persisted into 2016. Observations and numerical model output are used to document this warming and determine its origins. The coastal warming was mostly confined to the upper 100 m of the ocean and was manifested strongly in the two leading modes of upper ocean (0–100 m) temperature variability in the extratropical eastern Pacific. Observations suggest that the coastal warming in 2014 propagated into nearshore regions from the west while later indicating a warming influence that propagated from south to north into the region associated with the 2015–2016 El Niño event. An analysis of the upper ocean (0–100 m) heat budget in a Regional Ocean Modeling System (ROMS) simulation confirmed this scenario. The results from a set of sensitivity runs with the model in which the lateral boundary conditions varied supported the conclusions drawn from the heat budget analysis. Concerning the warming in the SFB, an examination of the observations and the heat budget in an unstructured-grid numerical model simulation suggested that the warming during the second half of 2014 and early 2016 originated in the adjacent California coastal ocean and propagated through the Golden Gate into the Bay. The finding that the coastal and Bay warming are due to the relatively slow propagation of signals from remote sources raises the possibility that such warming events may be predictable many months or even several seasons in advance.

Plain Language Summary The origins of the exceptionally warm water temperatures that developed off the California coast and in San Francisco Bay were studied using observations and computer model experiments. The coastal warming was mostly confined to the upper ocean. The coastal warming in 2014 was found to have moved into coastal waters from further offshore in the northeastern Pacific. Warming persisted into 2015–2016 as a warming influence from the south associated with the 2015–16 El Niño event in the tropical Pacific Ocean. The model experiments suggested that propagation of the warming signals from the west and north into the California coastal ocean and suggested that the warming in San Francisco Bay was found to have originated primarily in the adjacent California coastal ocean. The finding that the coastal and Bay warming are due to the relatively slow propagation of signals from remote sources raises the possibility that such warming events may be predictable many months or even several seasons in advance.

1. Introduction

The California coastal ocean is one of the nation's most important resources, both economically for its fisheries and ecologically for its diversity. It is home to several national marine sanctuaries including the Monterey Bay National Marine Sanctuary (montereybay.noaa.gov), a federally protected marine area offshore of California's central coast. Stretching from Marin County to Cambria, the sanctuary encompasses a shoreline length of 440 km and extends an average of 50 km from shore. Both fisheries and ecosystems are quite sensitive to changes in environmental conditions such as upper ocean temperature [McCabe *et al.*, 2016; Garfield *et al.*, 2015, 2016].

Beginning in early 2014, exceptionally warm temperatures developed across a wide area off the California coast as part of a broader pattern affecting the entire California Current system, and more generally much of the northeast Pacific. Near-surface positive temperature anomalies in the ocean exceeded 4°C in places and persisted at varying strength for much of the next 2 years [Gentemann *et al.*, 2017]. Warming in the northeast Pacific first appeared in late 2013 as an extensive, circular region of unusually high ocean temperatures (colloquially known as the "Pacific warm blob") attributed to higher than normal sea level pressures and weaker winds in the Gulf of Alaska that limited vertical mixing and equatorward advection of cool waters [Bond *et al.*, 2015]. Bond *et al.* [2015] found that these anomalies were the largest in the region since at least the 1980s. Brown and Fu [2000] also attributed the development of exceptionally warm SSTs in roughly the same offshore region during spring 1997 to weaker than normal winds in the Gulf of Alaska.

As the "blob" drifted toward the west coast of North America, the equatorial Pacific experienced an "aborted" El Niño in 2014 [Li *et al.*, 2015], followed in 2015 by the development of an exceptionally strong El Niño that had broad effects in the California Current [Levine and McPhaden, 2016; Jacox *et al.*, 2016]. It should be noted that impacts of this strong El Niño on the California Current system were not typical of those associated with canonical El Niño events [Frischknecht *et al.*, 2017] as the wind and precipitation anomalies differed from those expected during a strong El Niño [Paek *et al.*, 2017]. Nevertheless, these events exerted significant impacts on coastal ecosystems and North American climate [Medred, 2014; Bond *et al.*, 2015; Hartmann, 2015; Peterson *et al.*, 2015; Whitney, 2015; Hobday *et al.*, 2016; Siedlecki *et al.*, 2016; Zaba and Rudnick, 2016], such as causing a dramatic species range shift in the Gulf of Alaska during the summer and fall of 2014 [Medred, 2014] and delaying the onset of upwelling off the California coast during the summer of 2015 [Peterson *et al.*, 2015]. In perhaps the most dramatic ecosystem impact, McCabe *et al.* [2016] argued that an unprecedented California coastwide bloom of the toxigenic diatom *Pseudo-nitzschia* observed during spring 2015 was initiated by these anomalously warm ocean conditions. During this time, elevated toxins were measured in a number of stranded marine mammals and resulted in geographically extensive and prolonged closures of razor clam, rock crab, and Dungeness crab fisheries.

The effects of the exceptionally warm temperatures in the California coastal ocean were also felt in the San Francisco Bay estuary. The San Francisco Bay (SFB) is one of the largest estuaries in western North America and extends from the Golden Gate to the upstream portion of the San Joaquin-Sacramento River Delta southwest of Sacramento. SFB is a biological resource of substantial importance as it provides critical winter habitat for over a million migratory birds, a productive nursery for many species of juvenile fish and shellfish, and home for a vast diversity of plants and animals. SFB comprises four smaller bays: the least salty Suisun Bay, saltier San Pablo Bay west of Carquinez Strait, the saltiest Central Bay connected to the ocean at the Golden Gate, and the South Bay to the south of the Dumbarton Narrows (see Figure 5). As mentioned above, exceptionally warm temperatures first developed in 2014 across a wide area off the California coast to the west of SFB outside the Golden Gate. The SFB ecosystems are sensitive to changes in environmental conditions such as temperature. For example, the development of blooms of the harmful blue-green alga, *Microcystis aeruginosa* [Lehman *et al.*, 2008, 2013], in the upper Delta is likely related to increasing temperatures.

In this paper, we use observations, a ROMS-based numerical modeling system for the California coastal ocean, and an unstructured-grid numerical model for the SFB to understand the processes by which the California coastal warming developed and was transmitted to the SFB estuary. We begin in section 2 by describing the observational data sets and the two modeling systems (ROMS and SCHISM) used. We next describe in section 3 the observed warming, first on basin scales including the Pacific warm blob and El Niño, then in the California coastal ocean, and lastly in San Francisco Bay. Our description emphasizes the

warming propagation patterns and their influences on the California coast and SFB. We then explore in section 4 the origins of the California coastal ocean warming using the ROMS model. In particular, we focus on several distinct warming pulses and use results from the models to attribute the warming during these pulses to particular physical processes. In section 5, we similarly explore the physical processes behind the SFB warming using the SCHISM model. Lastly, in section 6, we present a summary and discussion.

2. Observational Data Sets and Numerical Models

2.1. Observational Data Sets

To characterize the warming of the upper ocean of the California coastal ocean, we use the following observational data sets: (1) temperature profiles from the M1 mooring (<http://www.cencoos.org/data/buoys/mbari/m1/info>) located in Monterey Bay (36.75°N, 122.03°W) and operated by the Monterey Bay Aquarium Research Institute (MBARI), (2) temperature profiles from the Scripps Institution of Oceanography (SIO) Spray gliders (<http://spraydata.ucsd.edu>) [Rudnick *et al.*, 2017], (3) ship CTD temperature profiles collected along the Oregon State University Newport Hydrographic Line off Newport, OR (44.6517°N) and off Trinidad, CA (41.053°N), (4) temperature profiles from a water quality mooring near San Diego operated by the City of San Diego (32.665°N, 117.326°W), and (5) gridded Argo float temperature fields (http://www.argo.ucsd.edu/Gridded_fields.html). Likewise for the SFB, we compile data from several sources: (1) the monthly ship survey with vertically sampled data collected by the U.S. Geological Survey (USGS) Water Quality of SFB program [Cloern and Schraga, 2016] (<http://sfbay.wr.usgs.gov/access/wqdata>) and (2) time series of near-surface temperature measurements at Tiburon (37.89166°N, 122.4463°W) and Carquinez (38.067°N, 122.23°W) stations (<http://sfbeams.sfsu.edu>) (see Figure 5). Except for the USGS data, which are monthly, we use 10 day averages in all subsequent presentations and analyses with these data and the unstructured grid model outputs (see below). Ten day averages were chosen as they were found to most clearly characterize the relatively large-scale, relatively long timescale (weeks to months) warming phenomena we are focusing on.

2.2. ROMS Model for the California Coastal Ocean

To explore the physical processes associated with the California coastal ocean warming, we use a Regional Ocean Modeling System (ROMS)-based California coastal modeling system. The ROMS configuration used consists of a single domain covering the entire California coast and its offshore waters to a distance of approximately 1000 km offshore at a resolution of 3 km. ROMS is a free-surface, hydrostatic, three-dimensional primitive equation regional ocean model [Haidvogel *et al.*, 2000; Shchepetkin and McWilliams, 2005, 2006; Marchesiello *et al.*, 2001]. The vertical discretization uses a stretched terrain-following coordinate (*S*-coordinate) on a staggered grid [Song and Haidvogel, 1994]. This allows the model to follow bottom topography with increased resolution in areas of interest, such as the thermocline and bottom boundary layers.

Lateral boundary conditions are generated using output from a global HYCOM model (<http://hycom.org>) and surface atmospheric forcing is derived from hourly output from operational forecasts performed with the NCEP NAM 5 km North American model (<http://www.emc.ncep.noaa.gov/index.php?branch=NAM>). The tidal forcing is added through lateral boundary conditions that are obtained from a global barotropic tidal model (TPXO.6) [Egbert and Erofeeva, 2002; Egbert *et al.*, 1994] that has a horizontal resolution of 0.25° and uses an inverse modeling technique to assimilate satellite altimetry cross-over observations. Similar, though nested, ROMS configurations have been successfully applied in the Monterey Bay [Chao *et al.*, 2009] and the Gulf of Alaska and Prince William Sound regions [Farrara *et al.*, 2013].

An essential component of the system is the data assimilation scheme used to generate the nowcast estimates of the three-dimensional ocean state. A two-step multiscale (MS) three-dimensional variational (3DVAR) data assimilation algorithm is used here. This MS-3DVAR scheme is a generalization of the 3DVAR methodology of Li *et al.* [2008a, 2008b] and is described in detail in Li *et al.* [2013, 2015a, 2015b]. The ROMS MS-3DVAR is designed to assimilate multiple types of observations simultaneously and reliably, while incorporating both the large-scale and small-scale impacts of the observations on the model fields, a distinct advantage over single-scale 3DVAR systems [Muscarella *et al.*, 2014]. This advantage is realized through the use of background error covariances of multidecorrelation length scales and by reducing inherent observational representativeness errors. In the implementation used here, the cost function set consists of two

components for large and small scales, each using own set of error covariances with different decorrelation length scales. The scheme is implemented sequentially from large to small scales. Of particular importance for applications such as this one, MS-3DVAR is effective in assimilating two of the most common types of ocean observations in the CA coastal region—sparse vertical profiles and high-resolution surface measurements—simultaneously. The following data sets were routinely available in near real-time and are assimilated by the ROMS MS-3DVAR system: gridded AVISO sea surface height data (<ftp.aviso.oceanobs.com>), high-frequency (HF) radar gridded surface current data (<http://hfrnet.ucsd.edu>), at 2 km and 6 km horizontal resolutions, vertical profiles of temperature and salinity from the Scripps Institution of Oceanography (SIO) gliders (<http://spraydata.ucsd.edu>) and the Monterey Bay Aquarium Research Institute (MBARI) M1 mooring (http://www.cencoos.org/data/buoys/mbari/m1tc_skyrocket), Advanced Very High Resolution Radiometer (AVHRR), Moderate Resolution Infrared Spectroradiometer (MODIS), and GOES satellite SSTs and ship SSTs (<ftp://usgodae.org>). An assimilation step is carried out every 6 h. A more detailed description of the system as well as a comprehensive validation of the model results using a number of observational data sets can be found in *Chao et al.* [2017]. A hindcast with data assimilation covering the period 1 January 2009 to 30 June 2016 has recently been completed and is one of the ROMS data sets used here.

2.3. SCHISM Model for San Francisco Bay (SFB)

To explore the processes associated with the SFB warming, we employ a modeling system based on the Semi-implicit Cross-scale Hydroscience Integrated System Model (SCHISM), an open-source community-supported modeling system using an unstructured grid [*Zhang et al.*, 2015; *Chao et al.*, 2017]. It uses a highly efficient semi-implicit finite-element/finite-volume method with an Eulerian-Lagrangian algorithm to solve the Navier-Stokes equations in hydrostatic form. The numerical algorithm mixes higher-order with lower-order methods, to obtain stable and accurate results in an efficient way. Mass conservation is enforced within the finite-volume transport algorithm. The model also incorporates wetting and drying of tidal flats. The SCHISM system has been extensively tested against standard ocean/coastal benchmarks and applied to a number of bays and estuaries around the world (see publications at http://ccrm.vims.edu/schism/schism_pubs.html), including the SFB and the larger San Francisco Bay Delta system by the California Department of Water Resources [*Ateljevich et al.*, 2014].

The SCHISM model runs performed here used a three-dimensional hydrostatic SFB configuration that includes a portion of the coastal ocean bounded by Point Reyes to the north and Half Moon Bay to the south. Horizontal resolution for this configuration ranges from approximately 1 km in the open ocean portion of the domain to as high as 10 m in the narrower channels inside the Bay. The average resolution within the Bay is about 100 m. In the vertical 23 terrain-following layers were used. The atmospheric forcing for the SCHISM model was taken from a 3 km Coupled Ocean Atmosphere Mesoscale Prediction System (COAMPS) regional atmospheric model run at Naval Research Laboratory in Monterey, CA [*Doyle et al.*, 2009]. Freshwater forcing from three major rivers (the Sacramento, San Joaquin, and Napa) and from the Coyote Creek at the lower end of the South Bay was prescribed using observed values of discharge and water temperature. Note that this SCHISM model configuration for SFB did not include data assimilation. At the open ocean lateral boundary, boundary conditions for temperature, salinity, and velocity were prescribed using output from the MS-3DVAR ROMS model described above [see also *Chao et al.*, 2017]. Note, however, that the SCHISM model configuration for SFB did not include data assimilation. As for ROMS, the SCHISM model was run for the seven and half year period from 1 January 2009 to 30 June 2016.

3. Observed Warming

In this section, we examine a variety of observations to characterize the warming on scales ranging from basin wide to the California coastal ocean to the San Francisco Bay. The analysis proceeds from the largest scale to smallest scales and emphasizes the potential impacts of large-scale propagating signals on the smaller scales.

3.1. North Pacific Warm “Blob” and Its Propagation

The spatial extent and evolution of the warming observed in the midlatitude eastern Pacific Ocean can be succinctly described using empirical orthogonal functions (EOFs) of the vertically averaged (0–100 m) upper ocean temperatures in the Argo gridded data set to obtain the leading modes of variability. This depth

range is consistent with previous reports on the vertical extent of the blob [Bond *et al.*, 2015] and our exploration of the Argo data set (see Figure 2). The EOF analysis was performed following Mo [2000] using the covariance matrix of the monthly-mean upper ocean temperature anomalies. Note that the climatology used to form the anomalies corresponds to the 2009–2015 mean seasonal cycle. This relatively short period for the construction of the climatology was used in order to ensure uniformity with the analysis of model simulations—which are by necessity relatively short—used to explore origins of the warming. To assess the representativeness of the climatological averages based on this period used (2009–2015), we have examined the upper ocean (0–100 m) temperatures in the HYCOM data and found that the 2009–2015 climatological averages are broadly representative of those obtained for climatologies based on data for other periods.

Figure 1 shows the first two EOFs in the Argo gridded data for the extratropical eastern Pacific Ocean (20°N–60°N, 100°W–180°W, Figures 1a and 1b) and the time series of the associated principal components (Figure 1c). The first mode (which accounts for 43% of the variability) is characterized by positive anomalies in the eastern half of the domain that extend to the coast in places and negative anomalies further offshore especially in midlatitudes. This pattern bears some resemblance to the pattern of warming and cooling associated with the Pacific Decadal Oscillation (PDO), which is the leading EOF of monthly SST anomalies in the entire extratropical North Pacific [Mantua *et al.*, 1997]. There are important differences, however, particularly the positive values in the southeastern portion of the domain seen in this first mode. The second mode of variability consists of an area of positive anomalies centered at approximately 150°W and 40°N surrounded by much weaker negative anomalies. This pattern strongly resembles the pattern in SST anomalies that developed in late 2013 described by Bond *et al.* [2015] and during spring 1997 described by Brown and Fu [2000]. Note that this second mode accounts for 15% of the variability.

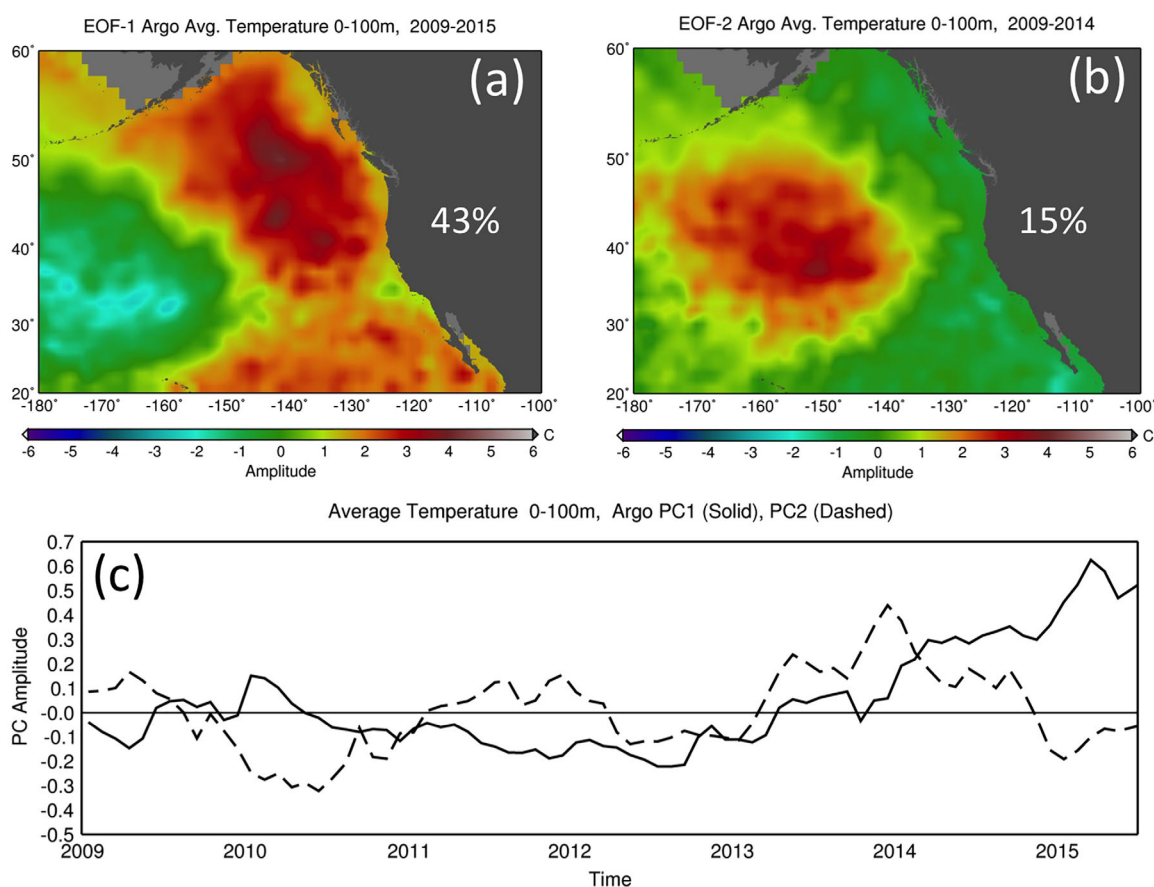


Figure 1. (a, b) Empirical orthogonal functions (EOFs) 1 and 2 of the upper ocean (0–100 m) average temperature (°C) from Argo float observations. (c) Principal components (PCs) 1 and 2 (solid and dashed lines, respectively).

The onset of warming manifests strongly in these two leading modes, as shown in the evolution of the associated principal components (PC1 and PC2, Figure 1c), with the second mode reaching a maximum positive peak in amplitude in late 2013 when the first mode is still quite weak, that immediately transitions to more of a mixed mode in early 2014 as the first mode becomes increasing positive. By later in 2014, the pattern comes to resemble more and more that of EOF1, as the strong positive values in PC1 associated with this mode persist and increase, while the values for PC2 decrease and eventually become negative. The transitions between these two modes and their roles in this warming have been discussed by *Di Lorenzo and Mantua* [2016].

To gain insight into the vertical extent of the warming pattern and its evolution, we examine longitude-depth cross sections from the Argo gridded data of the temperature anomalies averaged over the latitude band 30°N–45°N (Figure 2). Seasonal means are presented beginning with the season when the strong anomalies first appear, DJF 2013–2014 (Figure 2a), and for the subsequent three seasons: MAM 2014 (Figure 2b), JJA 2014 (Figure 2c), and SON 2014 (Figure 2d). Figure 2a shows that initially (DJF 2013–2014) the warm anomalies are present in a rectangular configuration well offshore, confined to longitudes between 130°W and 160°W and confined to depths shallower than about 75 m. By MAM 2014 (Figure 2b), the area of strong positive anomalies has moved east about 10–15° and expanded to depths greater than 100 m offshore. However, near the west coast the anomalies are shallower. During the subsequent two seasons (JJA and SON 2014, Figures 2c and 2d), the warm anomalies expand to reach depths of approximately 140 m while also becoming more confined to the near-coastal regions east of 140°W. Further west, the anomalies above 60 m become modestly negative by SON 2014. This evolution is broadly consistent with that of the associated PCs shown in Figure 1c in that it shows the warm anomalies that initially developed offshore (similar to the pattern in EOF-2) moving into the nearshore waters (similar to the pattern shown by EOF-1) during the period from winter 2013 to autumn 2014 (the period during which large positive values of PC2

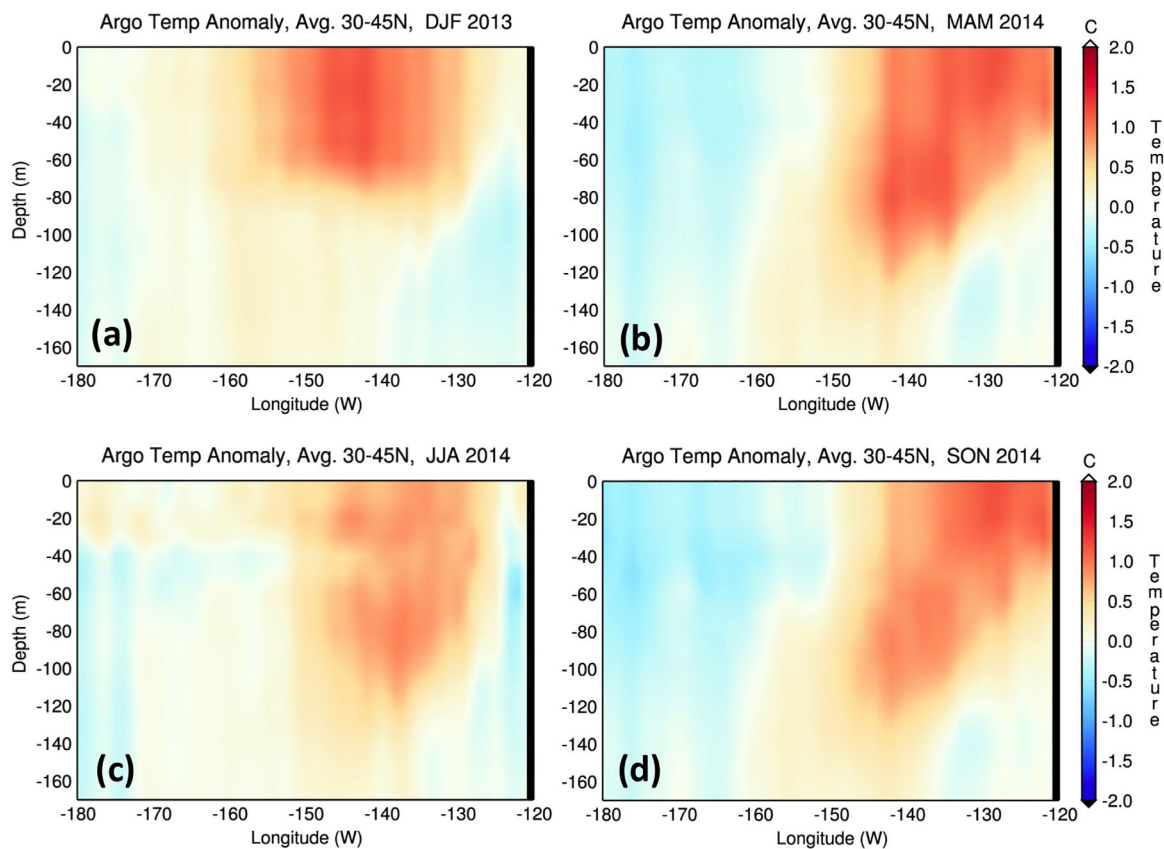


Figure 2. Depth-longitude plots of the vertically averaged (0–100 m) Argo temperature anomalies (°C), defined as the departure from the climatological mean annual cycle for the period 2009–2014, averaged over a latitudinal band from 30°N to 45°N during (a) December-January-February (DJF) 2013–2014, (b) March-April-May (MAM) 2014, (c) June-July-August (JJA) 2014, and (d) September-October-November (SON) 2014.

peak and then weaken, while strong positive values for PC1 develop). It is also consistent with the notion that the coastal warming was a result of oceanic processes causing the movement of the anomalously warm surface waters from the northeast Pacific Ocean to California.

3.2. Tropical Pacific El Niño Warming and Its Propagation

Subsequent to the genesis of the “warm blob” in the northeast Pacific and its propagation toward the west coast of North America, a major equatorial El Niño event developed during 2015 that lasted into 2016 [Levine and McPhaden, 2016; Jacox *et al.*, 2016]. Prior to this fully developed El Niño, conditions developed that at first seemed to indicate a building El Niño-Southern Oscillation (ENSO) event in 2014, but it never fully developed [Leising *et al.*, 2014]. El Niño-Southern Oscillation (ENSO) events have the potential to induce changes in the temperature structure along the west coast of North America [Norton and McLain, 1994]. These changes are, in part, produced by an extension of the oceanic mechanism underlying ENSO, namely, a large-scale equatorial Kelvin wave [Wyrtki, 1974; Busalacchi and O'Brien, 1981]. When this wave crosses the tropical Pacific and arrives at the South American coast, its energy splits: a portion reflects as a westward moving Rossby wave and the remaining energy travels toward each pole as coastal Kelvin waves [Clarke,

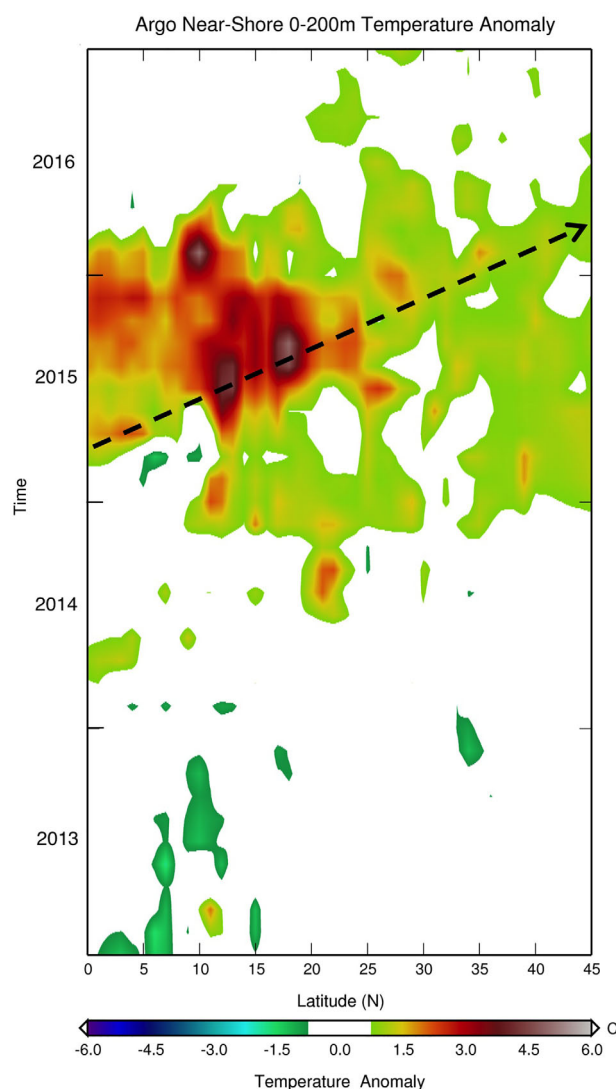


Figure 3. Monthly Argo depth-average (0–200 m) temperature anomalies ($^{\circ}\text{C}$) area-averaged for a longitude band extending 200 km offshore as a function of latitude and time. The black dashed arrow highlights the northward propagation of warm anomalies associated with the 2015–2016 El Niño as discussed in the text.

1983]. Numerical ocean models show that tropically forced Kelvin waves can be a significant source of interannual variability by inducing local processes that alter the nearshore temperature field along western America [Hurlburt *et al.*, 1976; McCreary, 1976; Pares-Sierra and O'Brien, 1989].

To track how equatorial forcing might have contributed to prolonging unusually warm temperatures observed off the California coast, we examined poleward propagation of temperature anomalies, with a focus on resolving the influence of the strong 2015 El Niño as well as any effect of the stalled 2014 El Niño. We examined temperature anomalies in the upper 200 m using the gridded Argo float temperature fields. Note that our averages here cover a larger depth range than those we used to characterize the “Blob” propagation as the tropical remote signal we are seeking here can extend to depths as great as 300–500 m [Norton and McLain, 1994]. Figure 3 shows the monthly mean temperature anomalies area-averaged over a longitude band extending 2° (approximately 200 km) offshore along the coast as a function of latitude from the equator to the central Oregon coast (45°N) and time from January 2013 to June 2016. Figure 3 shows these anomalies for a layer from 0 to 200 m that spans the range of the deeper anomalies shown in Figure 2.

Before 2015, anomalies are generally small—less than 0.5°C —everywhere, except later in 2014 in the north along the California and Oregon coasts. Strong warm anomalies first appear in the tropics in the spring

of 2015, then exhibit persistent, if somewhat erratic, poleward propagation along the coast, reaching California and Oregon in late 2015/early 2016 (Figure 3). *Norton and McLain* [1994] showed that remote forcing from the equatorial Pacific (ENSO), with apparent propagation rates of as slow as 30–50 km/d, is one of the major sources of interannual ocean temperature changes along the west coast of the United States especially during the fall and winter seasons. The observed time lag of around 9 months shown in Figure 3 is consistent with the arrival of equatorial signals off central California given these propagation rates [*Norton and McLain*, 1994].

Looking further back, a similar, but weaker pattern of poleward propagating warm anomalies can be seen along a parallel track beginning in Spring 2014 associated with the aborted El Niño event of that year and culminating in their arrival off California in early 2015 (Figure 3). We consider the propagation patterns revealed in Figure 3 to be consistent with remote forcing from the equatorial Pacific associated with the 2015–2016 ENSO event (and perhaps also the 2014–2015 event) and anticipate attributing any reinforcement of the warming in the California coastal region observed during late 2015/early 2016 (see section 4) to this remote ENSO influence.

3.3. California Coastal Ocean Warming

We describe next the warming observed along the California coast in the context of mean conditions during the 7 year period 2009–2015. The solid lines in Figure 4 show the time evolution of the observed upper ocean (0–100 m) temperature anomalies (base is the 2009–2015 mean annual cycle) obtained from seven different data sets gathered along and off the coast of California and southern Oregon.

The most prominent positive anomalies during this period generally develop during the first half of 2014 and persist at varying strengths through 2015 and into early 2016. Positive anomalies at some locations approach 2.5°C. At the southernmost location (the water quality mooring just offshore of San Diego shown by the red triangle in Figure 4), the anomalies in 2014 increase later and reach somewhat lower positive values than at the other locations before rebounding strongly during the fall of 2015. During 2014, persistent increases also come later at the nearshore M1 location and the two northernmost locations (the Trinidad line shown in green) and the Newport Hydrographic line [*Huyer et al.*, 2007] in Oregon (shown in red in Figure 4) where the anomalies do not peak until early 2015. The three other locations shown are the three SIO glider lines (from south to north: lines 90, 80, and 67). Note that for the Newport line, the Trinidad line and all the SIO glider lines we have averaged the anomalies at all points along the line to obtain the single time series displayed in Figure 4. In general, these three locations all show strong increases in temperatures during the first half of 2014. The curves for glider lines 90 and 80 show the positive anomalies developing in early 2014 and growing and persisting into early 2015 before weakening somewhat thereafter. The earlier appearance of persistent warming for the three glider lines that include an offshore component hints at the possibility that the warming influence in 2014 propagated from the west into the region.

Except for a brief springtime dip that is more prominent at the two nearshore stations (M1 and San Diego) during 2015, anomalies remain positive into 2016, and show a sometimes substantial rebound in either late 2015 or early 2016. The rebound tends to occur earlier (late 2015) at the southern locations (San Diego, Line 90) and later (early 2016) at the more northern locations (Line 67, Trinidad). This suggests a warming influence that propagated from south to north through the region. As will be seen below in Figure 8, there is an earlier mid-2015 increase in the anomalies in the central California coastal region that is primarily associated with anomalous upwelling. Such anomalous upwelling may also be playing a role in the warming further south, though we believe the primary driver in this region at this time is the remote influence of the 2015–2016 El Niño as we explain in section 4.

The dashed lines in Figure 4 show the colocated anomalies from the ROMS hindcast (note there is no dashed line for the Newport Line as the model domain does not include the Oregon coastal ocean). The hindcast, which includes the interannual variations in the atmospheric forcing and lateral boundary conditions, realistically reproduces the warming at all the locations. Note that there are discrepancies between the simulated and observed anomalies during the first 2 years of the simulation, perhaps due to adjustments related to the start of data assimilation in 2009.

3.4. San Francisco Bay Warming

We describe next the warming observed in San Francisco Bay during 2014–2016 with respect to the mean seasonal cycle during the period 2009–2015. To illustrate the warming, we examine first the anomalies in

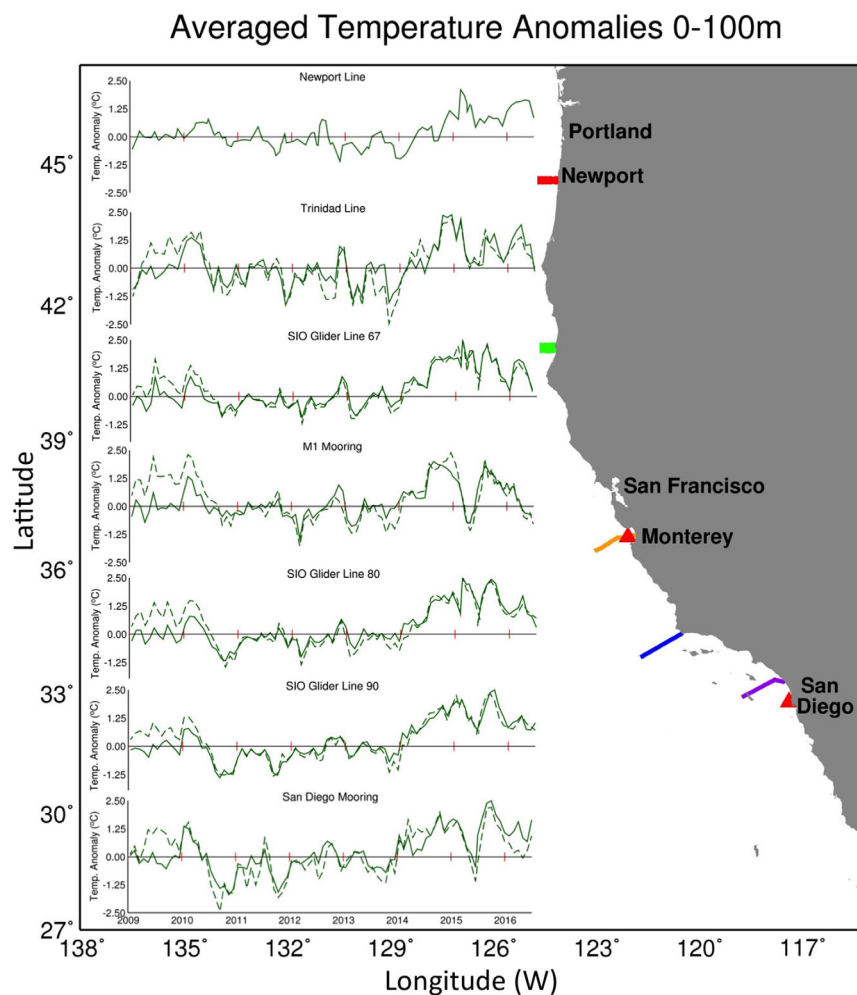


Figure 4. Time series of monthly-mean, depth-averaged (0–100 m) temperature anomalies ($^{\circ}\text{C}$; anomalies from the 2009–2015 means) for the period January 2009 to June 2016 from south to north: San Diego mooring (southernmost red triangle), Scripps glider transecting CalCOFI line 90 extending to 100 km offshore only for all gliders (purple line), Scripps glider transecting CalCOFI line 80 (blue line), M1 mooring (northernmost red triangle), Scripps glider transecting CalCOFI line 67 (orange line), and ship CTD observations near Trinidad, CA (green line) and near Newport, OR (red line). The dashed lines represent the anomalies from the CA ROMS hindcast run that includes data assimilation (see text for details).

the depth-average, station-average mean temperature observed at the 31 USGS stations used in this study (locations of these stations are shown by the purple triangles in Figure 5).

Figure 6a shows the evolution of the observed USGS depth-averaged temperature anomalies for the period January 2011 to June 2016 (solid line). These averaged anomalies present an overall picture of SFB-wide conditions. From the beginning of the period (1 January 2011) through mid-2012, temperatures are mostly cooler than the climatology. Beginning in early 2014, the observed temperatures become warmer than the climatology and remain warmer for the rest of the period. The most prominent positive anomalies in this time series occur in 2014 and early 2015 with an amplitude approaching 2°C . Except for a brief period in late 2015, the anomalies remain positive until the end of the period in June 2016. This SFB warming consists of several pulses. After the initial warming pulse in early 2014, there are several reinforcing pulses. We focus here on two of these reinforcing pulses, one that develops later in 2014 and the final one in early 2016. During the first pulse, anomalies increase from modestly negative values to greater than $+1^{\circ}\text{C}$. During the second pulse the averaged anomalies rise to greater than $+2^{\circ}\text{C}$. During the final pulse, anomalies rebound from slightly negative values to nearly $+1^{\circ}\text{C}$.

Also shown in Figure 6a are the colocated averaged anomalies from the SCHISM model simulation (dashed line); note that model anomalies were calculated in the same way as for the observations. In general, very

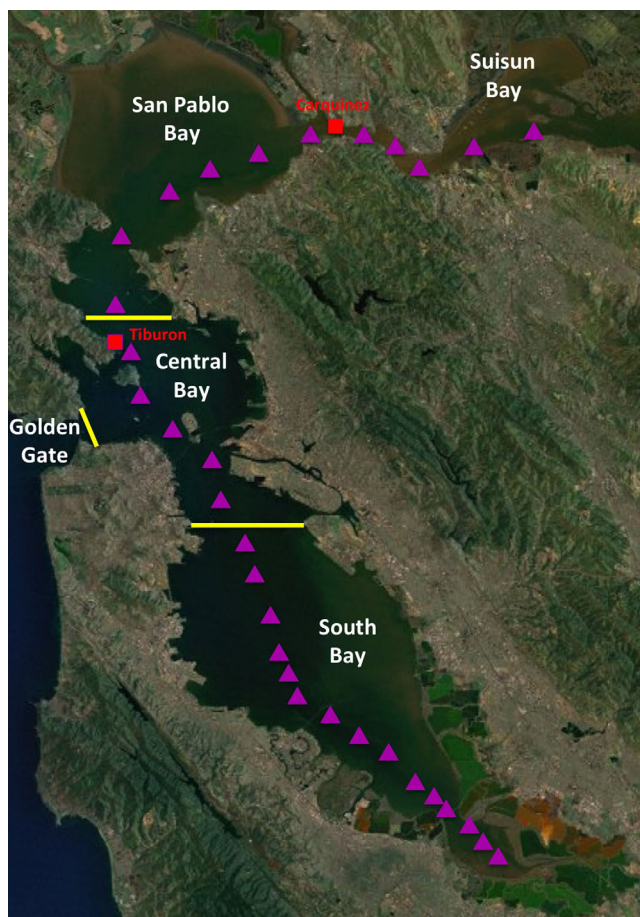


Figure 5. Map of the San Francisco Bay (SFB) region showing the locations of the 31 USGS water quality monitoring stations used in the analysis of the Bay warming as purple triangles and the locations of the Tiburon and Carquinez fixed stations as red squares with red labels. The yellow lines delineate the horizontal extent of the control volume for the SCHISM model heat budget calculations presented in the text.

are larger negative anomalies in early 2011 and 2012. Concerning the final pulse in early 2016, we note that at both Tiburon and Carquinez it is preceded by a brief period (of about 1 month) of strongly negative surface temperature anomalies and the pulse itself is quite strong with anomalies increasing from more than -2°C to nearly 3°C . In preparation for our model heat budget analyses, we have also examined the time series of depth-average temperature anomalies averaged for the USGS Central Bay stations only (not shown; the Central Bay stations are those within the area delineated by the yellow lines in Figure 5) and find the anomalies to be very similar to those presented in Figure 6a for all 31 stations. This is expected as SFB has strong tidal and diurnal wind mixing and indicates that we can use one or limited numbers of stations to track the entire SFB. In the following sections, we explore the potential contributions of the pathways identified in this section to warming in the California coastal ocean and SFB using the California coastal ROMS and SFB SCHISM models as diagnostic tools.

4. Origins of the California Coastal Ocean Warming

4.1. Heat Budget Analysis

In this section, we analyze the heat budget extracted from a nondata-assimilative configuration of the California coastal ROMS model run for the period from January 2009 through June 2016. We focus on the region off central California that includes the entrance to SFB. The budget analysis spans a control volume

good agreement is found between the simulated and observed temperature anomalies. In particular, there is good agreement on the timing and duration of the warming pulses during 2014–2016. Figures 6b and 6c show the higher temporal resolution observational time series (solid lines) of surface temperature anomalies at Tiburon in the Central Bay (Figure 6b) and Carquinez in the San Pablo Bay (Figure 6c). See the red squares in Figure 5 for the locations of these two stations. Note also that for the presentation of these time series we have averaged the original 6 min data into daily means. The evolution of the anomalies at Tiburon (Figure 6b) is in many ways similar to that for the USGS station average (Figure 6a) though with more high-frequency variations befitting its higher time resolution especially with regard to the warming pulses discussed above. There is also excellent agreement between the SCHISM model simulated daily mean anomalies (dashed line) and those observed, though some differences in timing occasionally occur. The evolution at Carquinez, which lies further inland and upstream of Tiburon and most of the USGS stations, shows some differences. In particular, the second 2014 warming pulse is not as well defined and occurs later in the year and there

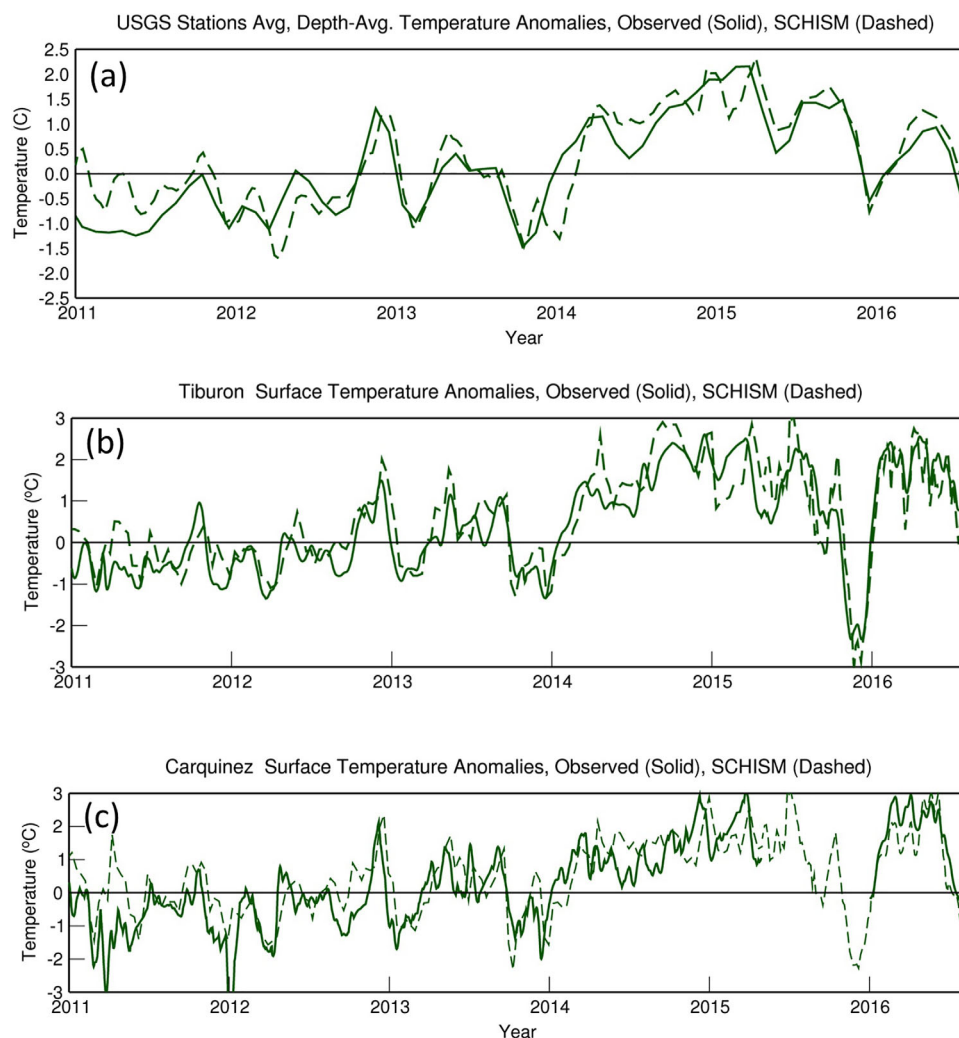


Figure 6. (a) Time series of monthly-mean, depth-averaged (0–10 m) temperature anomalies (°C; anomalies from the 2009–2015 means) for the period January 2011 to June 2016 for the 31 USGS station averaged temperatures within San Francisco Bay (see Figure 5 for the locations of the stations). (b, c) As in Figure 6a except for surface temperature anomalies at the Tiburon and Carquinez stations (see Figure 5 for locations).

that extends from the surface to a depth of 100 m in the region demarcated by the white box in Figure 7. Specifically, the upper ocean heat budget equation can be written as,

$$\Delta T = \Delta t (SHF + HA_w + HA_{NS} + VE), \quad (1)$$

where ΔT is the change in volume-average temperature, SHF represents net heating/cooling due to surface fluxes from the atmosphere acting on the 100 m deep layer, the HA terms represent the net horizontal temperature advection in the ocean through the western (HA_w) and the northern/southern (HA_{ns}) boundaries of the control volume, and VE the vertical entrainment. In the calculation, the ocean advection is determined by first integrating the ocean currents and potential temperatures from ocean surface to a depth of 100 m, and then calculating the horizontal temperature gradient and its dot product with the vertically integrated velocities. The analysis attributes anomalies in the monthly ($\Delta t = 1$ month) volume-average temperature changes (i.e., how much more warming or cooling is observed relative to average rates) to anomalies in the sum of the following budget terms: net surface atmospheric heat fluxes computed from the NAM forcing data used to drive the ROMS model, western lateral boundary heat fluxes, net northern and southern lateral boundary heat fluxes, and vertical heat fluxes across the bottom of the control volume (see equation (1)). Figure 8a shows that large positive anomalies in temperature change (i.e., unusual warming) within the control volume occurred during the early part of 2014, to a lesser extent during the latter half of 2014, a brief

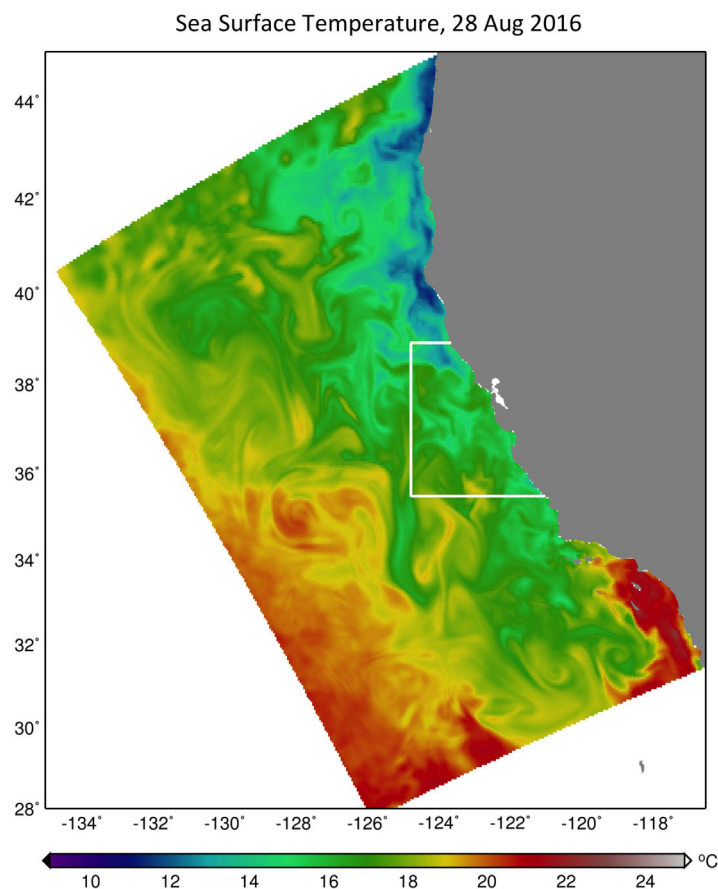


Figure 7. Daily mean ROMS sea surface temperatures for 28 August 2016 on the CA-3km model domain (colored region). The white box delineates the horizontal area used to define the control volume for the ROMS heat budget calculations presented in the text.

period in mid-2015, and lastly during early 2016. We focus here on two of these warming pulses (indicated by the shading in Figure 8a), the first covering the period December 2013 to March 2014, and the fourth covering the period December 2015 to March 2016. Figure 8b schematically summarizes the mean contributions of the various fluxes to anomalous temperature changes in the control volume over each of the two focal warming pulses.

We examine in Figure 8a anomalies in the monthly volume-average temperature changes (black line) and attribute them to anomalies in the sum of the following budget terms: net surface atmospheric heat fluxes (red line) computed from the NAM forcing data used to drive the ROMS model, the western lateral boundary heat fluxes (green line), the net northern and southern lateral boundary heat fluxes (dashed green line), and the vertical heat fluxes (purple line) at the bottom of the volume at a depth of 100 m.

The thick solid line shows the anomalies in the temperature changes within the control volume and indicate that large positive values occurred during the early part of 2014, to a lesser extent during the latter half of 2014, a brief period in mid-2015 and lastly during early 2016. We focus here on two of these warming pulses, the first covering the period from December 2013 to March 2014, and the last covering the period from December 2015 to March 2016. The light brown shading in Figure 8 highlights these two periods. Note that the warming during mid-2015 is separated from the warming during the December 2015 to March 2016 by a period of cooling and is also distinct from the later warming in that it is characterized by a strong contribution to the warming from the vertical entrainment term (see Figure 8).

Focusing first on the surface atmospheric fluxes (red), Figure 8a shows that these fluxes are strongly positive at the beginning of the first warming pulse and remain positive, while generally decreasing in magnitude for the rest of this warming pulse. Throughout the second warming pulse, the atmospheric fluxes are negative, though they again decrease in magnitude. This suggests that atmospheric fluxes are contributing to the anomalous warming during the first warming pulse, but not during the second. This is depicted schematically in Figure 8b. Next, we note that the vertical heat fluxes are relatively small during each of the two warming pulses, suggesting they are not a primary driver of the warming. Finally, we examine the ocean heat fluxes through the lateral boundaries of the box in Figure 8. The fluxes through the western boundary (green solid line) are large and positive during most of the first warming pulse in early 2014, but are very small during the second pulse in early 2016. In contrast, the net fluxes through the northern and southern boundaries of the box are relatively small (though positive) during the first warming pulse, but very large during the second warming pulse. This difference is shown schematically in Figure 8b, which displays the means during the two warming pulses of each of the terms. During the first warming pulse, the mean

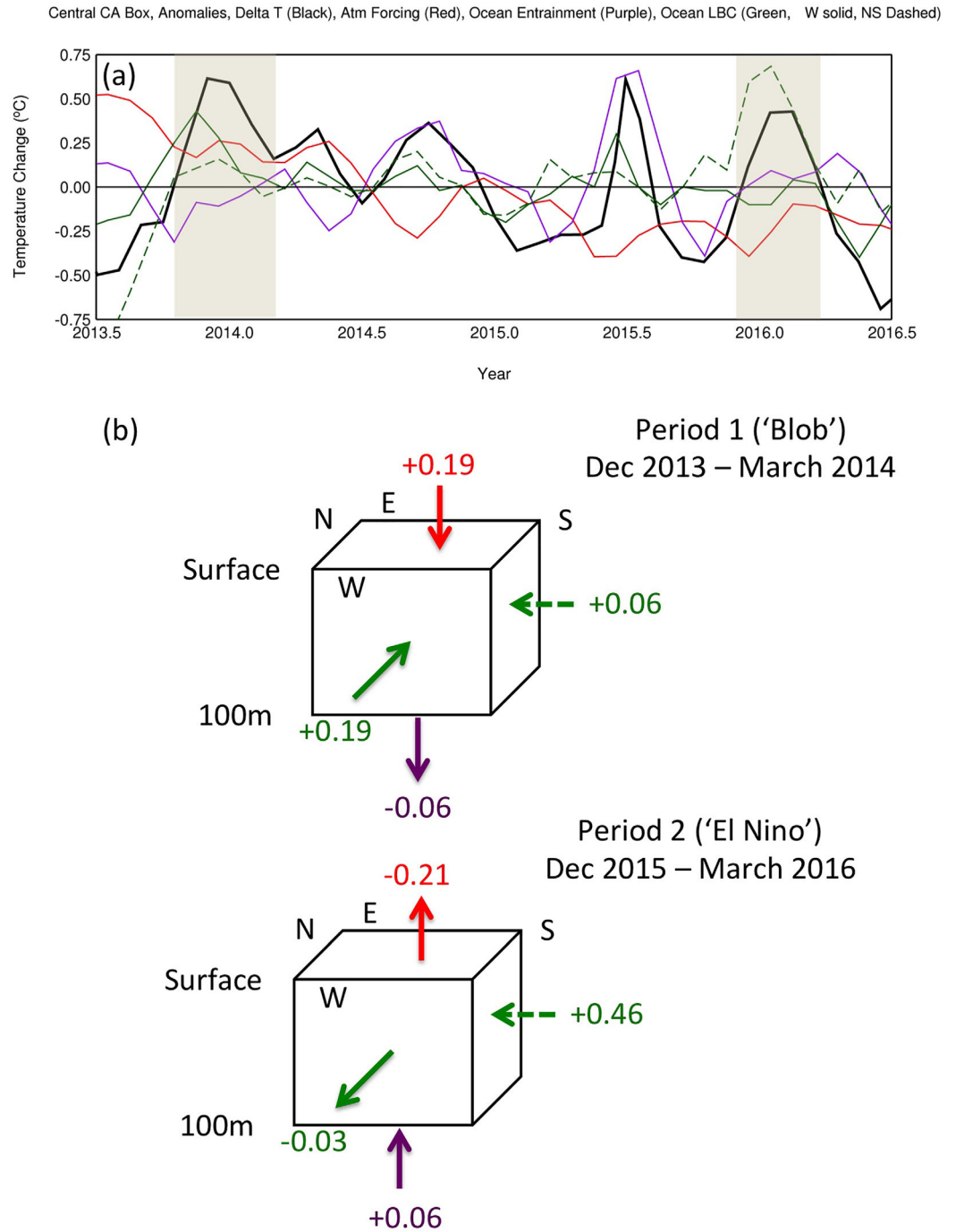


Figure 8. (a) Terms in ROMS heat budget for the coastal CA box shown in Figure 7: monthly volume-average temperature changes (°C, black), surface atmospheric forcing (red), ocean entrainment (purple), ocean lateral boundary forcing (green solid), north-south lateral lateral boundary forcing (green dashed). The light brown shading denotes the periods during which the two warming pulses (“Blob” and “El Nino”) discussed in the text develop. (b) Schematic depicting the mean values of the terms in the heat budget during the two periods highlighted in Figure 8a. The arrows are color-coded to correspond to the curves in Figure 8a. Note that the arrows show the direction of the fluxes only, they are not scaled to the magnitude of the heat fluxes they represent.

atmospheric fluxes and mean western lateral boundary fluxes contribute equally to the warming (+0.19°C/10 days), while the other terms are small. During the second warming pulse, the mean atmospheric flux is decidedly negative (−0.21°C/10 days), the net N-S flux contributes the major portion of the warming (+0.46°C/10 days) and the other terms are relatively small. This picture for the first warming pulse is consistent with a substantial contribution to this pulse from the transport of anomalously warm “blob” waters

from the adjacent northeastern Pacific Ocean as seen in the analysis of the Argo temperature data presented in Figures 1 and 2. For the second warming pulse, the larger contribution from the north-south lateral boundaries strongly suggests that this warming is associated with the poleward propagation of an ENSO signal as hinted at in Figure 3. We do not attempt to determine here how this ENSO influence is transmitted. However, given the hints in Figure 3 we believe it is most likely associated with coastally trapped waves. Anomalous alongshore advection may also be contributing further south but we feel it is unlikely to be the primary mechanism this far north as there is limited evidence for such advection outside of the Southern California Bight region [see Rudnick *et al.*, 2017] and the southern boundary of our “budget” box is north of the Bight. In contrast to the first and fourth warming pulses, the second and third warming pulses appear to be driven less by fluxes across the lateral boundaries of the control volume, but rather to reflect warming of the control volume due to vertical fluxes of heat from depth that exceed losses to the atmosphere (Figure 8a). Both pulses occur after the establishment of deeper warm anomalies along the coast, and potentially reflect changes in the characteristics of waters entrained to the surface layer through upwelling at the coastal margin, or through mixing or curl-driven upwelling over the domain of the control volume. In both cases, we note that although the magnitudes of positive fluxes across the lateral boundaries of the control volume are small relative to the vertical flux, lateral fluxes enhance warming during each of the intervening warming pulses.

4.2. Model Sensitivity Runs

To further evaluate whether and how the pathways identified in section 3 potentially contribute to the warming of California coastal ocean waters in 2014–2016, we performed runs with three alternative configurations of the ROMS model. Each configuration is designed to test the sensitivity of model results to particular differences in the specification of lateral boundary conditions that convey the influence of different sources of remote forcing to the model domain. The first of the three sensitivity runs was identical to the control except that climatological lateral boundary conditions (BCs) were used at the “western” boundary instead of the interannually varying standard HYCOM boundary condition (see colored area in Figure 7 for full domain of the ROMS CA model); the second used climatological lateral BCs at the “southern” boundary; the third used climatological lateral BCs everywhere. Note that the atmospheric forcing was identical in all four runs. Figure 9 summarizes the results, showing the time evolution of the volume-averaged temperature anomalies in the four runs (see box in Figure 7, depth is 0–100 m: control, thick solid line; climatological western BC, thick dashed line; climatological southern BC, thin dashed line; climatological BC all, thin solid line).

The control run shows the anomalies decreasing for most of the second half of 2013 before increasing fairly rapidly and persistently into spring 2014 then leveling off. This is the first warming pulse identified above during the period December 2013 to March 2014. Anomalies then increase again during the second half of 2014, reaching their peak value of nearly 2.5°C very early in 2015. The anomalies then slowly and irregularly decrease during most of 2015 before increasing again during the period December 2015 to March 2016, which is the second warming pulse described above. In the sensitivity run that excludes interannual

Central CA Box, ROMS 0-100m Temp Anom (Thick Solid), Clim W (Thick Dashed), Clim NS (Thin Dashed), Clim Both (Thin Solid)

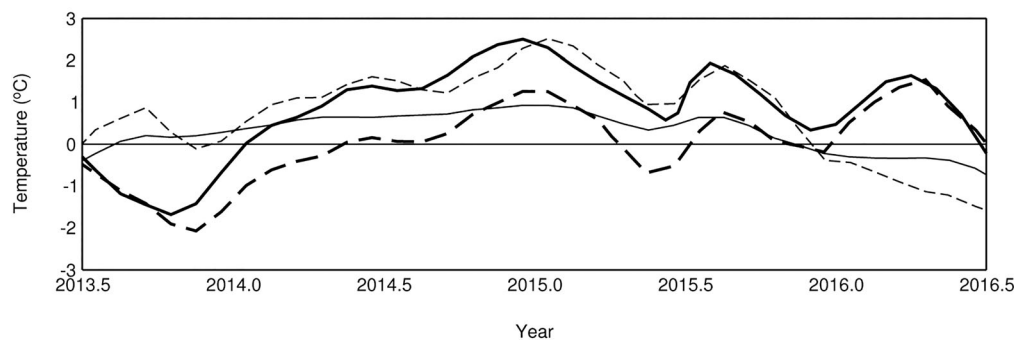


Figure 9. Coastal central CA box temperature anomalies (°C) for the ROMS run with no data assimilation (thick solid line), climatological lateral boundary forcing at the north and south boundaries (thin dashed line), climatological lateral boundary forcing at the western boundary (thick dashed line), and climatological lateral boundary forcing at all boundaries (thin solid line).

variations in the “western” lateral ocean boundary forcing (thick dashed line) the warming during the first pulse is weaker and anomalies do not become positive until late in 2014, suggesting that the western boundary heat fluxes were an important component during this first pulse. On the other hand, the warming during the second pulse is very similar to that seen in the control run, suggesting an insignificant role for the western boundary heat fluxes during this second pulse. This result is consistent with the results from the heat budget analysis presented above that suggested a substantial contribution to this pulse from the transport of anomalously warm “blob” waters from the adjacent northeastern Pacific Ocean as seen in the analysis of the Argo temperature data presented in Figures 1 and 2.

In the sensitivity run that excludes interannual variations in the “southern” lateral ocean boundary forcing (thin dashed line), the warming during the first pulse is well reproduced, while that during the second pulse is not. This result is consistent with the results from the heat budget analysis presented above that suggested a substantial contribution from the north-south lateral boundary and thus, that this warming is associated with the poleward propagation of an ENSO signal as shown in Figure 3. Lastly, the run with climatological lateral BCs at all boundaries (thin solid line) does not clearly reproduce either one of the warming pulses, instead showing smaller variations with time and anomalies that lie within a range of $\pm 0.75^{\circ}\text{C}$.

5. Origins of the San Francisco Bay Warming

In an attempt to gain insight into the origins of the SFB warming during the second warming pulse in late summer/early fall 2014 (see section 3.5), we analyzed 10 day mean maps of SST anomalies from the SCHISM model simulations (Figure 10).

During this second warming pulse, we find qualitative evidence from the SCHISM model simulation of warming appearing first in the coastal ocean and then propagating into the Bay through the Golden Gate (Figure 10). During the first ten-day period shown (Figure 10a) the positive anomalies within and just outside the Bay are around 1°C with somewhat larger positive anomalies further offshore. By the second period twenty days later, strong positive anomalies of $3\text{--}4^{\circ}\text{C}$ have developed throughout the coastal ocean area outside the Bay and have begun extending through the Golden Gate and into the Central Bay (Figure 10b). Over the two subsequent periods (Figures 10c and 10d), anomalies inside the Bay continue to increase as warmer waters appear to spread north and south from the Central Bay into San Pablo and South Bays. Anomalies in the open ocean part of the domain remain strongly positive. Maps of SST from satellite observations were also examined (not shown) but showed numerous gaps in coverage due to cloud cover. Nevertheless, the observed satellite surface temperature maps show a broadly similar evolution, though with less spatial and temporal continuity due to the frequent gaps in coverage. This evolution suggests that the warming of the SFB during the latter half of 2014 resulted from an intrusion of warmer-than-normal water from the adjacent coastal ocean and through the Golden Gate.

To more quantitatively estimate the relative contributions of oceanic and atmospheric heat fluxes to each warming pulse, we analyzed the heat budget for a control volume bounded on the east by the coast and on the north, south, and west by the yellow lines in Figure 5; this region approximately corresponds to the USGS definition of the Central SFB (<http://sfbay.wr.usgs.gov/access/wqdata>). Horizontally, this volume is bounded on the east by the coastline and on the west by the narrow strait at the Golden Gate. Vertically, the volume extended from the surface to the model bottom, which generally ranges from 10 to 20 m below the surface in this part of the Bay. This analysis follows the same methodology used in the ROMS heat budget analysis (see equation (1)), except that heat transport at the bottom of the volume, which is the bottom of the Bay, was assumed to be zero ($VE = 0$). In all cases, 10 day means were used noting that calculations based on shorter averaging windows (daily or hourly) sufficient to resolve synoptic or tidal processes did not yield substantially different results. In a manner consistent with the coherent responses to warming observed throughout SFB, lateral heat fluxes at the northern and southern boundaries were much smaller than the fluxes at the surface and western (ocean) boundaries, and are not considered further.

To compute the heat transports at the remaining lateral boundaries (west), data from the SCHISM model simulation were used. The net heat flux from the atmosphere into the volume was computed using the COAMPS atmospheric model forcing. Figure 11a shows the anomalies resulting from the change in either transports at the western boundary (dashed line) or the surface atmospheric fluxes (thin solid line) along

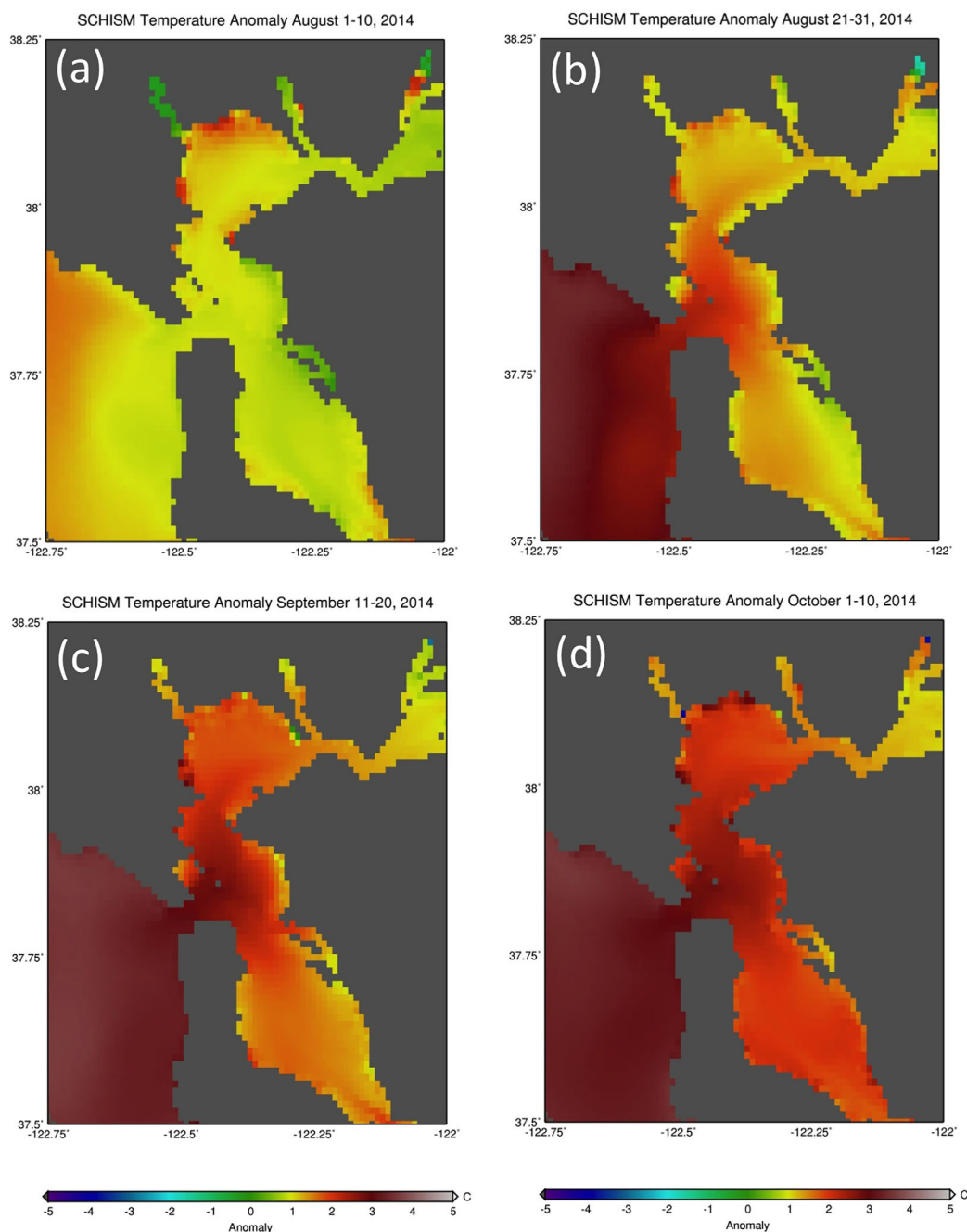


Figure 10. Ten day average surface water temperature anomalies (°C) as simulated by the SCHISM model (see text for details). Means for the periods (a) 1–10 August 2014, (b) 21–30 August 2014, (c) 11–20 September 2014, and (d) 1–10 October 2014.

with the anomalies in the 10 day mean temperature changes in the Central Bay volume (thick solid line). The light brown shading in Figure 11a highlights the time periods covered by each of the three warming pulses. During the first warming pulse in early 2014, positive anomalies in both the surface atmospheric heat fluxes (for the first half of the pulse) and the western boundary heat transports contribute to the increase in temperature anomalies. This is shown schematically in Figure 11b, which displays the means of the two terms during the two warming pulses and reveals that during the first pulse (December 2013 to April 2014) the positive western boundary fluxes are about twice as large as the positive heat fluxes from the atmosphere. During the second pulse (August 2014 to November 2014), however, the anomalies in the atmospheric fluxes are strongly negative, likely as a result of larger than normal losses of heat (latent and

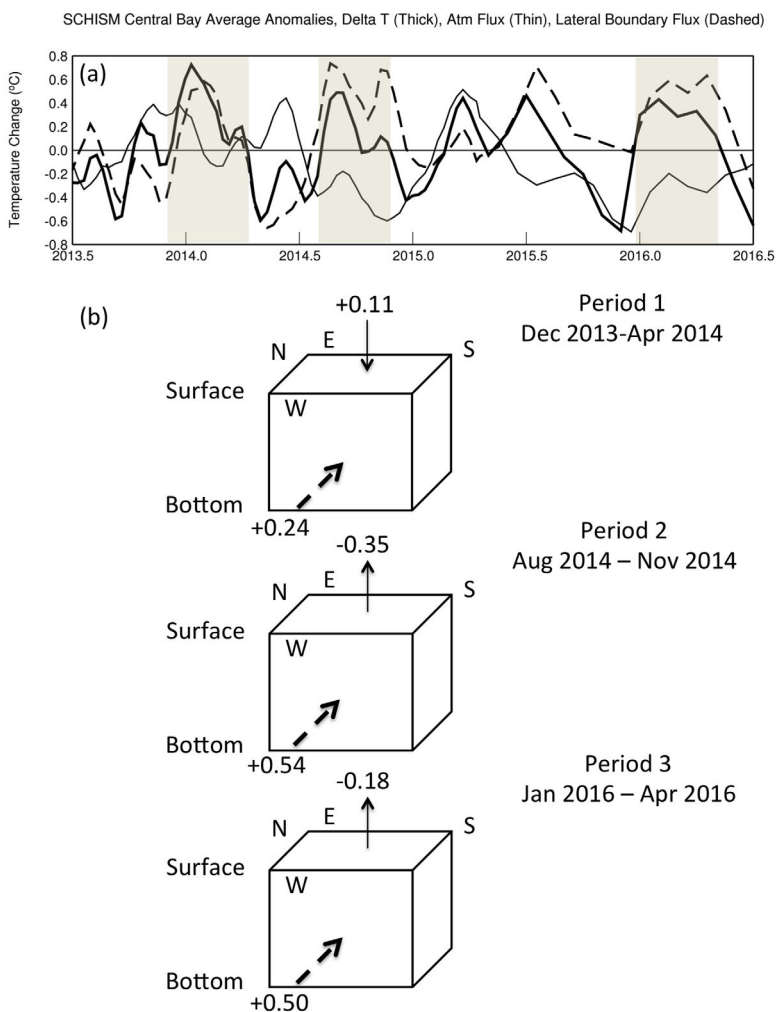


Figure 11. (a) For the period 1 July 2013 to 30 June 2016, anomalies (from the 2005–2015 mean seasonal cycle) in 10 day volume-averaged temperature changes (°C, thick solid line) in the central Bay volume delineated by the yellow lines in Figure 5 and anomalies in key terms in the heat budget for this volume contributing to these changes. The thin solid line shows anomalies in the fluxes from the atmosphere and the dashed line the anomalies in the heat flux at the western lateral boundary of the volume. The light brown shading denotes the periods during which the primary warming pulses discussed in the text develop. (b) Schematic depicting the mean values of the terms in the heat budget during the three periods highlighted in Figure 11a, thin solid arrows show the direction of fluxes from the atmosphere and thick dashed arrows show the direction of fluxes through the western lateral boundary. Note that the arrows are not scaled to the magnitude of heat flows.

infrared) from the anomalously warm SFB waters. As these anomalies remained negative throughout the entire second half of 2014, it is clear that the warming of the Bay during the second pulse was caused solely by the strong positive anomalies in the western boundary heat transport beginning in August and continuing through November 2014. For this period, the substantially negative mean heat fluxes from the atmosphere ($-0.35^{\circ}\text{C}/10$ days) are overwhelmed by even larger positive mean fluxes from the western boundary ($+0.54^{\circ}\text{C}/10$ days). During the third and final warming pulse we selected (in early 2016), the story is largely the same as for the second pulse, as the mean atmospheric fluxes are again negative ($-0.18^{\circ}\text{C}/10$ days), while the western boundary fluxes are large and positive ($+0.50^{\circ}\text{C}/10$ days).

6. Summary and Discussion

During 2014–2016 exceptionally warm water temperatures developed and persisted across a wide area off the California coast and within San Francisco Bay. Observations and numerical model output were used to document this anomalous warming and its origins. This prolonged coastal warming developed within the context of broader warming throughout the northeast Pacific [Bond *et al.*, 2015] that first appeared in late

2013 and the exceptionally strong El Niño that developed during 2015 [Levine and McPhaden, 2016; Jacox *et al.*, 2016]. Spatially, the northeast Pacific and California coastal warming were manifested strongly in the two leading modes of upper ocean (0–100 m) temperature variability in the extratropical eastern Pacific as seen in gridded Argo data. The second mode, whose pattern resembles that of the region of strongly positive sea surface temperature anomalies described by Bond *et al.* [2015], peaked first in late 2013/early 2014 and was followed by a stronger more persistent peak in the first mode, which bears some resemblance to the PDO, in 2014 and 2015. We note that the first mode also strongly resembles the anomaly pattern identified by Fiedler and Mantua [2017] as typical for CCS warming events they identified as arising from concurrent changes in forcing at local scales (northeast Pacific) and of tropical origin (El Niño). In the vertical, the gridded Argo temperature data reveal that the maximum depth covered by strong positive anomalies expands from around 80–140 m as the anomalies moved eastward toward the coast during 2014. Beginning in spring 2015, strong deep-layered (0–200 m) positive temperature anomalies were observed in the eastern tropical Pacific that subsequently showed an erratic, but persistent poleward propagation along the coast, reaching central California seven to nine months later in late 2015/early 2016. We consider this propagation to be evidence of remote forcing of the California coastal ocean from the equatorial Pacific associated with the 2015–2016 ENSO event.

Our analysis of basin-scale temperature anomalies in the Argo data set identified two pathways by which remotely generated warm anomalies arrived to and persisted in California's waters from 2014 to 2016. The first is the eastward propagation of unusually warm surface waters formed in the northeast Pacific during 2013 [Bond *et al.*, 2015] (Figures 1 and 2) that appears to have a stronger influence in the north. The second is poleward propagation of equatorial signals that, by virtue of influencing vertical structure (e.g., offshore propagating depression of the thermocline), tended to have a stronger signature away from the coast and somewhat deeper in the water column.

To characterize the California coastal ocean warming, temperature anomalies in the upper 100 m of the ocean were used. This depth range was chosen based on our analysis of the Argo temperature anomalies, which showed that strong positive anomalies during this event were mostly confined to this part of the ocean. Positive anomalies approaching 2.5°C were found at a number of locations along the coast for much of the latter half of 2014 and early 2015. The results for glider lines 67, 80, and 90 show the positive anomalies developing beginning in early 2014 and growing and persisting into early 2015 before weakening somewhat thereafter. The earlier appearance of persistent warming for the three glider lines that include an offshore component hints at the possibility that the warming influence in 2014 that propagated from the west into the region, consistent with the Argo vertical cross sections (Figure 2). Except for a brief spring 2015 dip at the two nearshore stations (M1 and San Diego), anomalies remained positive into 2016, and showed a substantial rebound in either late 2015 or early 2016. The rebound tended to occur earlier (late 2015) at the southern locations and later (early 2016) at the northern locations. This suggests a warming influence that propagated from south to north through the region.

For the SFB, both the depth-averaged USGS Bay-wide data and the surface temperatures from Tiburon and Carquinez capture the onset of persistent warm temperatures in early 2014, the strengthening of the anomalies—in some cases exceeding 2°C—in late 2014 into 2015, and, following a brief bout of cooler conditions in late 2015, a sharp restoration of unusually warm conditions in 2016 (Figure 6). Together these data sets suggest a coherent evolution of warming in SFB, in which subsequent warming pulses reinforced the effects of an initial warming pulse in early 2014.

To confirm the impressions gleaned from our analysis of the observations, we then analyzed the upper ocean (0–100 m) heat budget in a nondata assimilative ROMS simulation for a volume of the central California coastal ocean. This analysis revealed that during the first warming pulse in 2014, the mean atmospheric fluxes (as suggested by Zaba and Rudnick [2016]) and mean western lateral boundary fluxes contributed equally to the warming, confirming a substantial contribution to the 2014 warming from the transport of anomalously warm “blob” waters from the adjacent northeastern Pacific Ocean as suggested by the analysis of the Argo temperature data. During the second “rebound” warming pulse in late 2015/early 2016, the mean atmospheric flux is decidedly negative, and it is the positive net heat flux through the southern boundary that contributes the major portion of the warming, as the other terms are relatively small. For this second warming pulse, the larger contribution from the southern lateral boundary strongly suggests that this warming is associated with the poleward propagation of an ENSO signal. We note here that the budget

calculations performed using atmosphere and ocean model fluxes are subject to uncertainties in the simulation of the air-sea fluxes in the NAM atmospheric model and ocean lateral boundary fluxes in the ROMS ocean model.

This warming by poleward advection at the height of the El Niño is consistent with the findings of *Lynn and Bograd* [2002] during 1997–1998 and *Rudnick et al.* [2017] during 2015–2016. The above results are also in general agreement with recent findings of *Fiedler and Mantua* [2017] based on statistical analysis of correlations between CCS SST anomalies and indices of forcing in the northeast Pacific and along the Equator. In particular, the analysis of ARGO temperature anomalies and heat budgets document processes consistent with their conclusion that the 2014 warming event was largely driven by changes in the northeast Pacific and local forcing, which might reflect indirect tropical influence [see also *Di Lorenzo and Mantua*, 2016]. Moreover, we document how El Niño compounded warming in the CCS during 2015, which *Fiedler and Mantua* [2017] identified as a strong “CCS warming with El Niño” event, despite unusually strong (for El Niño conditions) upwelling winds off southern and central California during 2015 [*Jacox et al.*, 2016; *Frischknecht et al.*, 2017].

To further demonstrate the robustness of these findings, we performed a set of sensitivity runs with the ROMS model in which the lateral boundary conditions imposed varied. The overall picture obtained from these runs supports the conclusions drawn from the heat budget analysis for these two warming pulses. Specifically, in the runs where the western boundary forcing does not contain the northeast Pacific warming signal, the warming during the first warming pulse is substantially weaker than in the control run and runs that do not include the El Niño warming signal at the southern boundary do not reproduce the warming seen in the control run during the second warming pulse.

The same result has been derived independently from the zooplankton time series at Newport. There, the copepods that occurred during autumn 2014 to spring 2015 were species known to inhabit water to the west of Oregon/Northern California Current, in the eastward flowing North Pacific Transition Zone. However, beginning in late April/May 2015, species known to inhabit water to the south of Oregon appeared suggesting a change in hydrography, namely, from the influence of “Blob” water in 2014–early 2015 to El Niño from mid-2015 through 2016. A similar result was found for copepods and euphausiids at Trinidad.

An analysis of the spatial evolution of the surface temperature anomalies in the SFB and adjacent coastal ocean during the warming pulse in the second half of 2014 suggested that the main cause of the warming was the transport of anomalously warm water from the adjacent Pacific Ocean. An examination of the heat budget in the SCHISM model for a control volume in the central SFB supported this conjecture and suggested that the final warming pulse in 2016 was very similar in that it was also primarily driven by the transport of anomalously warm water from the adjacent Pacific Ocean.

Coastal and estuarine ecosystems are sensitive to changes in environmental conditions such as temperature. Being able to model the temperature linkages between the coastal ocean and SFB offers the hope of developing predictive capabilities for warming events such as the one studied here as well as anomalous cold events. Moreover, the results presented here showing that substantial components of the warming in the both the California coastal ocean and SFB are due to the relatively slow (months) propagation of signals from remote sources raises the possibility that such changes may be predictable many months to even several seasons in advance.

References

- Ateljevich, E., K. Nam, Y. Zhang, R. F. Wang, and Q. Shu (2014), Bay-Delta SELFE calibration overview, in *Methodology for Flow and Salinity Estimates in the Sacramento-San Joaquin Delta and Suisun Marsh, 35th Annu. Prog. Rep.*, Dep. of Water Resour., Calif. Nat. Resour. Agency, Sacramento, Calif.
- Bond, N. A., M. F. Cronin, H. Freeland, and N. Mantua (2015), Causes and impacts of the 2014 warm anomaly in the northeast Pacific, *Geophys. Res. Lett.*, 42, 3414–3420, doi:10.1002/2015GL063306.
- Brown, R. G., and L.-L. Fu (2000), An examination of the spring 1997 mid-latitude east Pacific sea surface temperature anomaly, *Atmos. Ocean*, 38(4), 577–599.
- Busalacchi, A. J., and J. J. O'Brien (1981), Interannual variability of the equatorial Pacific in the 1960s, *J. Geophys. Res.*, 86, 10,901–10,907.
- Chao, Y., et al. (2009), Development, implementation and evaluation of a data-assimilative ocean forecasting system off the central California coast, *Deep Sea Res., Part II*, 56, 100–126, doi:10.1016/j.dsr2.2008.08.011.
- Chao, Y., J. D. Farrara, H. Zhang, Y. J. Zhang, E. Ateljevich, F. Chai, C. O. Davis, R. Dugdale, and F. Wilkerson (2017), Development, implementation and validation of a modeling system for the San Francisco Bay and estuary, *Estuarine Coastal Shelf Sci.*, 194, 40–56, doi:10.1016/j.ecss.2017.06.005.
- Clarke, A. J. (1983), The reflection of equatorial waves from oceanic boundaries, *J. Phys. Oceanogr.*, 13, 1193–1207.

Acknowledgments

The research of Y. Chao and J. Farrara at Remote Sensing Solutions is supported by NOAA's Integrated Ocean Observing System (IOOS) Community Coastal and Ocean Modeling Testbed (COMT) program through the Southeastern Universities Research Association (SURA), the NOAA Integrated Ocean Observing System (IOOS) through Alaska Ocean Observing System (AOOS) as well as a subcontract from Oregon State University funded by NASA Interdisciplinary Science program Award NNX14AD79G (to C. O. Davis at Oregon State University). The research of Y. Chao and H. Zhang at the University of California at Los Angeles (UCLA) is supported by the NOAA Integrated Ocean Observing System (IOOS) through Southern California Coastal Ocean Observing System (SCCOOS) and Central and Northern California Ocean Observing System (CeNCOOS). Support from the UCLA Joint Institute for Regional Earth System Science and Engineering (JIFRESSE) is gratefully acknowledged. CeNCOOS (via MBARI) makes available the temperature profiles from the M1 mooring (<http://www.cencoos.org/data/buoys/mbari/m1/info>). The temperature profile data from the Scripps Institution of Oceanography (SIO) Spray gliders can be found at <http://spraydata.ucsd.edu>. The Argo Program is part of the Global Ocean Observing System. The Argo data were collected and made freely available by the International Argo Program (<http://www.argo.ucsd.edu>, <http://argo.jcommops.org>). The Argo gridded data used in the present study is obtained from http://www.argo.ucsd.edu/Gridded_fields.html. The United States Geological Survey data used here was downloaded from <https://sfbay.wr.usgs.gov/access/wqdata/>. James Doyle of the Naval Research Laboratory, Monterey graciously provided the COAMPS atmospheric model output, which is also available at http://www.usgodae.org/pub/outgoing/fnmoc/models/coamps/calif/cencoos/cencoos_4km/. The rest of the data used are listed in the references.

- Cloern, J. E., and T. S. Schraga (2016), USGS measurements of water quality in San Francisco Bay (CA), 1969–2015, U.S. Geological Survey Data Release, U.S. Geol. Surv., doi:10.5066/F77Q5ZPR.
- Di Lorenzo, E., and N. Mantua (2016), Multi-year persistence of the 2014/15 North Pacific marine heatwave, *Nat. Clim. Change*, *6*, 1042–1047, doi:10.1038/nclimate3082.
- Doyle, J. D., Q. Jiang, Y. Chao, and J. D. Farrara (2009), High-resolution real-time modeling of the marine atmospheric boundary layer in support of the AOSNII field campaign, *Deep Sea Res., Part II*, *56*, 87–99, doi:10.1016/j.dsr2.2008.08.009.
- Egbert, G. D., and S. Y. Erofeeva (2002), Efficient inverse modeling of barotropic ocean tides, *J. Atmos. Oceanic Technol.*, *19*, 183–204.
- Egbert, G. D., A. F. Bennett, and M. G. G. Foreman (1994), TOPEX/POSEIDON tides estimated using a global inverse model, *J. Geophys. Res.*, *99*, 24,821–24,852.
- Farrara, J. D., et al. (2013), A data-assimilative ocean forecasting system for the Prince William Sound and an evaluation of its performance during Sound Predictions 2009, *Cont. Shelf Res.*, *63*, S193–S208, doi:10.1016/j.csr.2012.11.008.
- Fiedler, P. C., and N. J. Mantua (2017), How are warm and cool years in the California Current related to ENSO?, *J. Geophys. Res. Oceans*, *122*, 5936–5951, doi:10.1002/2017JC013094.
- Frischknecht, M., M. Münnich, and N. Gruber (2017), Local atmospheric forcing driving an unexpected California Current System response during the 2015–2016 El Niño, *Geophys. Res. Lett.*, *44*, 304–311, doi:10.1002/2016GL071316.
- Garfield, T., et al. (2015), California Current integrated ecosystem assessment, current system report, State of the Calif., Sacramento, Calif. [Available at http://www.pcouncil.org/wp-content/uploads/2016/02/D1a_NMFS1_2015_IEA_SoCC_FINAL_MAR2016BB.pdf]
- Garfield, T., et al. (2016), California Current integrated ecosystem assessment, current system report, State of the Calif., Sacramento, Calif. [Available at http://www.pcouncil.org/wp-content/uploads/2016/02/D1a_NMFS1_2015_IEA_SoCC_FINAL_MAR2016BB.pdf]
- Gentemann, C. L., M. R. Fewings, and M. Garcia-Reyes (2017), Satellite sea surface temperatures along the west coast of the United States during the 2014–2016 northeast Pacific marine heatwave, *Geophys. Res. Lett.*, *44*, 312–319, doi:10.1002/2016GL071039.
- Haidvogel, D. B., H. G. Arango, K. Hedstrom, A. Beckmann, P. Malanotte-Rizzoli, and A. F. Shchepetkin (2000), Model evaluation experiments in the North Atlantic Basin: Simulations in nonlinear terrain-following coordinates, *Dyn. Atmos. Oceans*, *32*, 239–281.
- Hartmann, D. (2015), Pacific sea surface temperature and the winter of 2014, *Geophys. Res. Lett.*, *42*, 1894–1902, doi:10.1002/2015GL063083.
- Hobday, A. J., et al. (2016), A hierarchical approach to defining marine heatwaves, *Prog. Oceanogr.*, *141*, 227–238, doi:10.1016/j.pocean.2015.12.014.
- Hurlburt, H. E., J. C. Kindle, and J. J. O'Brien (1976), A numerical simulation of the onset of El Niño, *J. Phys. Oceanogr.*, *6*, 621–631.
- Huyer, A., P. A. Wheeler, P. T. Strub, R. L. Smith, R. Letelier, and P. M. Kosro (2007), The Newport line off Oregon—Studies in the northeast Pacific, *Prog. Oceanogr.*, *75*(2), 126–160.
- Jacox, M. G., E. L. Hazen, K. D. Zaba, D. L. Rudnick, C. A. Edwards, A. M. Moore, and S. J. Bograd (2016), Impacts of the 2015–2016 El Niño on the California Current System: Early assessment and comparison to past events, *Geophys. Res. Lett.*, *43*, 7072–7080, doi:10.1002/2016GL069716.
- Lehman, P. W., G. Boyer, M. Satchwell, and S. Waller (2008), The influence of environmental conditions on the seasonal variation of *Microcystis* cell density and microcystins concentration in San Francisco Estuary, *Hydrobiologia*, *600*, 187–204.
- Lehman, P. W., K. Marr, G. L. Boyer, S. Acuna, and S. J. Teh (2013), Long-term trends and casual factors associated with *Microcystis* abundance and toxicity in San Francisco Estuary and implications for climate change impacts, *Hydrobiologia*, *718*, 141–158.
- Levine, A. F. Z., and M. J. McPhaden (2016), How the July 2014 easterly wind burst gave the 2015–2016 El Niño a head start, *Geophys. Res. Lett.*, *43*, 6503–6510, doi:10.1002/2016GL069204.
- Leising, A. W., et al. (2014), State of the California Current in 2013–14: El Niño looming, CalCOFI report, vol. 55, 37 pp., CalCOFI: California Cooperative Oceanic Fisheries Investigations La Jolla, Calif.
- Li, J., et al. (2015), A comparative study on the dominant factors responsible for the weaker-than-expected El Niño event in 2014, *Adv. Atmos. Sci.*, *32*, 1381–1390, doi:10.1007/s00376-015-4269-6.
- Li, Z., Y. Chao, J. C. McWilliams, and K. Ide (2008a), A three-dimensional variational data assimilation scheme for the regional ocean modeling system, *J. Atmos. Oceanic Technol.*, *25*, 2074–2090.
- Li, Z., Y. Chao, J. C. McWilliams, and K. Ide (2008b), A three-dimensional variational data assimilation scheme for the regional ocean modeling system: Implementation and basic experiments, *J. Geophys. Res.*, *113*, C05002, doi:10.1029/2006JC004042.
- Li, Z., Y. Chao, J. D. Farrara, and J. C. McWilliams (2013), Impacts of distinct observations during the 2009 Prince William Sound field experiment: A data assimilation study, *Cont. Shelf Res.*, *63*, supplement, S209–S222, doi:10.1016/j.csr.2012.06.018.
- Li, Z., J. C. McWilliams, K. Ide, and J. D. Farrara (2015a), A multiscale variational data assimilation scheme: Formulation and illustration, *Mon. Weather Rev.*, *143*, 3804–3822, doi:10.1175/MWR-D-14-00384.1.
- Li, Z., J. C. McWilliams, K. Ide, and J. D. Farrara (2015b), Coastal Ocean data assimilation using a multi-scale three-dimensional variational scheme, *Ocean Dyn.*, *65*, 1001–1015, doi:10.1007/s10236-015-0850-x.
- Lynn, R. J., and S. J. Bograd (2002), Dynamic evolution of the 1997–1999 El Niño-La Niña cycle in the southern California Current System, *Prog. Oceanogr.*, *54*(1–4), 59–75, doi:10.1016/S0079-6611(02)00043-5.
- Mantua, N. J., S. R. Hare, Y. Zhang, J. M. Wallace, and R. C. Francis (1997), A Pacific decadal climate oscillation with impacts on salmon, *Bull. Am. Meteorol. Soc.*, *78*, 1069–1079.
- Marchesiello, P., J. C. McWilliams, and A. F. Shchepetkin (2001), Open boundary conditions for long-term integration of regional ocean models, *Ocean Modell.*, *3*, 1–20.
- McCabe, R. M., B. M. Hickey, R. M. Kudela, K. M. Lefebvre, N. G. Adams, B. D. Bill, F. M. Gulland, and V. L. Trainer (2016), An unprecedented coastwide toxic algal bloom linked to anomalous ocean conditions, *Geophys. Res. Lett.*, *43*, 10,366–10,376, doi:10.1002/2016GL070023.
- McCreary, J. (1976), Eastern tropical response to changing wind systems: With application to El Niño, *J. Phys. Oceanogr.*, *6*, 632–645.
- Medred, C. (2014), Unusual species in Alaska waters indicate parts of Pacific warming dramatically, *Alaska Dispatch News*, 14 Sept. [Available at <http://www.adn.com/article/20140914/unusual-species-alaska-waters-indicate-parts-pacific-warming-dramatically>.]
- Mo, K. C. (2000), Relationships between interdecadal variability in the Southern Hemisphere and sea surface temperature anomalies, *J. Clim.*, *13*, 3599–3610.
- Muscarella, P. A., M. J. Carrier, and H. E. Ngodock (2014), An examination of a multi-scale three-dimensional variational data assimilation scheme in the Kuroshio Extension using the naval coastal ocean model, *Cont. Shelf Res.*, *73*, 41–48, doi:10.1016/j.csr.2013.11.009.
- Norton, J. G., and D. R. McLain (1994), Diagnostic patterns of seasonal and interannual temperature variation off the west coast of the United States: Local and remote large-scale atmospheric forcing, *J. Geophys. Res.*, *99*, 16,019–16,030.
- Paek, H., J.-Y. Yu, and C. Qian (2017), Why were the 2015/16 and 1997/98 Extreme El Niños different?, *Geophys. Res. Lett.*, *44*, 1848–1856, doi:10.1002/2016GL071515.
- Pares-Sierra, A., and J. J. O'Brien (1989), The seasonal and interannual variability of the California current system: A numerical model, *J. Geophys. Res.*, *94*, 3159–3180.

- Peterson, W., M. Robert, and N. Bond (2015), The warm Blob continues to dominate the ecosystem of the Northern California Current, PICES Press, 23(2).
- Rudnick, D. L., K. D. Zaba, R. E. Todd, and R. E. Davis (2017), A climatology of the California Current System from a network of underwater gliders, *Prog. Oceanogr.*, *154*, 64–106, doi:10.1016/j.pocean.2017.03.002.
- Shchepetkin, A. F., and J. C. McWilliams (2005), The regional ocean modeling system: A split-explicit, free-surface, topography-following-coordinate ocean model, *Ocean Modell.*, *9*, 347–404.
- Shchepetkin, A. F., and J. C. McWilliams (2006), Computational kernel algorithms for fine-scale, multi-process, long-time oceanic simulations, in *Handbook of Numerical Analysis: Computational Methods for the Atmosphere and the Oceans*, edited by R. Temam and J. Tribbia, pp. 121–183, Elsevier, Amsterdam, Netherlands.
- Siedlecki, S., E. Bjorkstedt, R. Feely, A. Sutton, J. Cross, and J. Newton (2016), Impact of the Blob on the northeast Pacific Ocean biogeochemistry and ecosystems, *US CLIVAR Variations*, *14*, 7–12.
- Song, Y. T., and D. B. Haidvogel (1994), A semi-implicit ocean circulation model using a generalized topography-following coordinate system, *J. Comput. Phys.*, *115*, 228–244.
- Whitney, F. A. (2015), Anomalous winter winds decrease 2014 transition zone productivity in the NE Pacific, *Geophys. Res. Lett.*, *42*, 428–431, doi:10.1002/2014GL062634.
- Wyrtki, K. (1974), Equatorial currents in the Pacific 1950 to 1970 and their relations to the trade winds, *J. Phys. Oceanogr.*, *4*, 372–380.
- Zaba, K. D., and D. L. Rudnick (2016), The 2014–2015 warming anomaly in the Southern California Current System observed by underwater gliders, *Geophys. Res. Lett.*, *43*, 1241–1248, doi:10.1002/2015GL067550.
- Zhang, Y., E. Ateljevich, H-C. Yu, C-H. Wu, and J. C. S. Yu (2015), A new vertical coordinate system for a three-dimensional unstructured-grid model, *Ocean Modell.*, *85*, 16–31.